

University of Nebraska - Lincoln

DigitalCommons@University of Nebraska - Lincoln

---

Mechanical & Materials Engineering Faculty  
Publications

Mechanical & Materials Engineering,  
Department of

---

2022

## Symmetric or asymmetric glide resistance to twinning disconnection?

Mingyu Gong

Houyu Ma


Kunming Yang

Yue Liu

Jian-Feng Nie

*See next page for additional authors*

Follow this and additional works at: <https://digitalcommons.unl.edu/mechengfacpub>

 Part of the [Mechanics of Materials Commons](#), [Nanoscience and Nanotechnology Commons](#), [Other Engineering Science and Materials Commons](#), and the [Other Mechanical Engineering Commons](#)

---

This Article is brought to you for free and open access by the Mechanical & Materials Engineering, Department of at DigitalCommons@University of Nebraska - Lincoln. It has been accepted for inclusion in Mechanical & Materials Engineering Faculty Publications by an authorized administrator of DigitalCommons@University of Nebraska - Lincoln.

---

**Authors**

Mingyu Gong, Houyu Ma, Kunming Yang, Yue Liu, Jian-Feng Nie, and Jian Wang

## ARTICLE OPEN



## Symmetric or asymmetric glide resistance to twinning disconnection?

Mingyu Gong<sup>1,4</sup>, Houyu Ma<sup>1,4</sup>, Kunming Yang<sup>1</sup>, Yue Liu<sup>1</sup>, Jian-Feng Nie<sup>2</sup> and Jian Wang<sup>3</sup>

Successive gliding of twinning disconnections (TDs) creates three-dimensional twins in parent crystal and accommodates shear deformation. It is generally recognized that TD is subject to the same Peierls stress as it glides forward or backward because of its dislocation character and the twofold rotation symmetry of the twin plane. Based on atomistic simulations, we demonstrate that the glide of TDs may be subject to a symmetric or asymmetric resistance corresponding to step character, symmetric resistance for A/A type steps but asymmetric resistance for A/B type steps, where A and B represent crystallographic planes in twin and matrix. Furthermore, we experimentally demonstrate that the asymmetric resistance results in asymmetric propagation and growth of twins in Mg alloys.

npj Computational Materials (2022)8:168; <https://doi.org/10.1038/s41524-022-00855-y>

## INTRODUCTION

Disconnection is the elementary carrier for phase transformation and twinning<sup>1,2</sup>. Disconnection has dislocation character with Burgers vector  $\mathbf{b}$  and step character with height  $h$ , described as  $(\mathbf{b}, h)^{2-4}$ . The motion of disconnections on the habit plane not only accommodates shear displacement but also reorients crystal into new orientation or new phase<sup>1-6</sup>. A dislocation is subject to the same Peierls stress as it moves forward or backward when the glide plane holds a two-fold rotation symmetry about its normal axis<sup>7</sup>. This is referred to as symmetric resistance to dislocation motion. Dislocation motion accommodates shear displacement on slip plane, generating plastic deformation. Following the understanding to dislocation motion, it is widely recognized that a disconnection is also subject to symmetric resistance because it has dislocation character and the rational twin plane holds a two-fold rotation symmetry. Obviously, the step character associated with disconnections was totally ignored in evaluating the moving direction dependence of glide resistance.

Phase transformation is generally operated by two different disconnections (i.e.  $\mathbf{b}_1$  and  $\mathbf{b}_2$  on the left and right) with the same signed Burgers vector to relieve the coherency stress<sup>5,8</sup> with a tilt wall left at the origin. Burgers vector of  $\mathbf{b}_1$  and  $\mathbf{b}_2$  affects their mobility, which could be revealed by the shape of a thin domain that does not fully traverse the grain<sup>1,9</sup>. If  $\mathbf{b}_1$  and  $\mathbf{b}_2$  have different Burgers vector, they are likely to manifest different mobilities since their core structures differ. Correspondingly, a thin domain will exhibit lath shape. Alternatively, if  $\mathbf{b}_1$  and  $\mathbf{b}_2$  have the same Burgers vector but the opposite line sense (i.e., a closed disconnection loop), a lenticular-shaped domain will be expected because of the same mobility of both disconnections. However, a lath-shaped domain is generally developed even if  $\mathbf{b}_1$  and  $\mathbf{b}_2$  have the same mobility, because misfit strain along the interface will be reduced in one direction but increase in another direction<sup>10</sup>. The accumulated misfit strain will impede the gliding of disconnection in one direction. A comprehensive description and discussion can be found in ref. <sup>11</sup>.

Deformation twinning is accomplished through nucleation and motion of twinning disconnections (TDs)<sup>5,12,13</sup>. Corresponding to the mirror symmetry about twin plane, twinning does not create misfit strain along the twin plane (coherent twin boundary, CTB). Elementary TD ( $\mathbf{b}_T$ ) and its complementary TD ( $\mathbf{b}_C$ ) have opposite sign where  $\mathbf{b}_T + \mathbf{b}_C$  is a full lattice translation vector along the twinning shear direction<sup>12</sup>. When both  $\mathbf{b}_T$  and  $\mathbf{b}_C$  are activated, the same argument as the case of phase transformation is applied for the propagation and shape of twins. However,  $\mathbf{b}_C$  is rarely activated because it has a bigger Burgers vector, higher formation energy and lower mobility, compared with  $\mathbf{b}_T$ . Therefore, elementary TD is the only TD during twinning.

Twins are three-dimensional entities, as schematically illustrated in Fig. 1 for simplicity.  $\mathbf{b}_T$  (or  $(\mathbf{b}_T, h_0)$ ) and  $-\mathbf{b}_T$  (or  $(-\mathbf{b}_T, -h_0)$ ) glide toward the twinning shear ( $\boldsymbol{\eta}_1$ ) and the opposite direction ( $-\boldsymbol{\eta}_1$ ), and toward the lateral sides along the  $-\boldsymbol{\lambda}$  and  $\boldsymbol{\lambda}$  directions, achieving twin propagation/growth. Since normal  $\mathbf{K}_1$  is a two-fold rotation axis for twin plane, the mobility of  $\mathbf{b}_T$  and  $-\mathbf{b}_T$  on  $\pm\mathbf{K}_1$  twin planes is generally treated to be the same, and the twin shall exhibit a lenticular shape with symmetric twin tips, as illustrated in Fig. 1a, b. However,  $\mathbf{b}_T$  and  $-\mathbf{b}_T$  on  $\pm\mathbf{K}_1$  twin planes may have different Peierls barrier. First, with steps character<sup>14-16</sup>, a TD core may relax on a slanted plane to form a coherency disclination<sup>17-19</sup> and does not retain the two-fold symmetry about the rotation axis  $\mathbf{K}_1$ . Second, the glide of a TD is accompanied with atomic shuffling that may not retain the two-fold rotation symmetry<sup>3,20</sup>. Thus, twins may grow into lath shape with asymmetric tips, as illustrated in Fig. 1d, e.

When viewing a twin from 'bright side' (BS, along  $\boldsymbol{\lambda}$  direction),  $\mathbf{b}_T$  and  $-\mathbf{b}_T$  are edge type, a twin may grow a lenticular shape with symmetric twin tips (Fig. 1b) or a lath shape with asymmetric twin tips (Fig. 1e) depending on whether the TD relaxes into a coherency disclination on a slanted plane. When viewing a twin from 'dark side' (DS, along  $\boldsymbol{\eta}_1$  direction),  $\mathbf{b}_T$  and  $-\mathbf{b}_T$  are screw type, the same Peierls stress is expected as it glides in the  $-\boldsymbol{\lambda}$  and  $\boldsymbol{\lambda}$  directions because of the two-fold symmetry about the rotation axis  $\mathbf{K}_1$ <sup>21,22</sup>. Twins may grow a lenticular shape with symmetric tips in DS view, as shown in Fig. 1c, f. In addition, big step or facet

<sup>1</sup>State Key Lab of Metal Matrix Composites, School of Materials Science and Engineering, Shanghai Jiao Tong University, Shanghai 200240, P.R. China. <sup>2</sup>Department of Materials Science and Engineering, Monash University, Clayton, VIC 3800, Australia. <sup>3</sup>Department of Mechanical & Materials Engineering, University of Nebraska-Lincoln, Lincoln, NE 68583, USA. <sup>4</sup>These authors contributed equally: Mingyu Gong, Houyu Ma. ✉email: [yliu23@sjtu.edu.cn](mailto:yliu23@sjtu.edu.cn); [jianwang@unl.edu](mailto:jianwang@unl.edu)

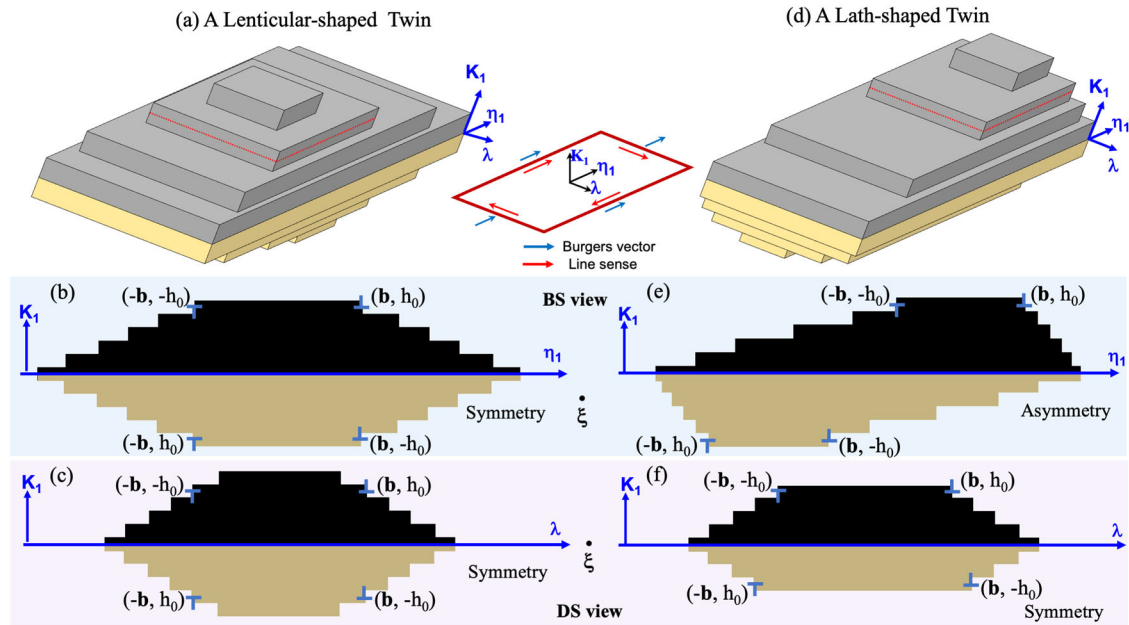


**Fig. 1 Schematics of three-dimensional (3D) twin shapes.** **a** Lenticular-shaped and **d** lath-shaped twins. Lenticular-shaped twin exhibits symmetric twin shape in **b** BS and **c** DS view. Lath-shaped twin exhibits an asymmetry twin shape in **e** BS view and quasi-symmetric twin shape in **f** DS view.

associated with pileup of multiple TDs may form and influence propagation/growth of twins.

The aforementioned argument demands a comprehensive understanding and quantitative analysis of Peierls stress for TD or step as it moves in the  $\pm\eta_1$  and  $\pm\lambda$  directions. Moreover, 3D microscopy characterization of twins with focus on twin tips and twin shapes can provide direct evidence of Peierls stress's effect on deformation twinning. In what follows, we conducted atomistic simulations and microscopy characterization of  $\{10\bar{1}1\}$  twins in Mg to examine our argument.  $\{10\bar{1}2\}$  twins<sup>12,14,15</sup> in Mg alloys are also characterized and compared to  $\{10\bar{1}1\}$  twins.

## RESULTS

### Glide resistance of twinning disconnection

The structures and energetics of elementary TDs associated with  $\{10\bar{1}1\}$  twinning, and their kinetics along different directions can be assessed by atomistic calculations<sup>14,23</sup>, which are also applied to studies of TDs associated with  $\{10\bar{1}2\}$  and  $\{11\bar{2}2\}$  twinning<sup>24,25</sup>. Figure 2a schematically shows TDs along CTBs ( $\pm\mathbf{K}_1$  twin planes). For two TD loops on CTBs, four TDs ( $-\mathbf{b}_T, h_0$ ) and ( $\mathbf{b}_T, -h_0$ ), ( $\mathbf{b}_T, h_0$ ) and ( $-\mathbf{b}_T, -h_0$ ) are equivalent according to the crystallography of the twin. However, the core of TDs may not relax on twin plane. Figure 2b shows the atomic structures of a TD dipole on  $\mathbf{K}_1$  twin plane in BS view. TDs are edge type and the step height  $h_0$  involves four atomic planes<sup>14,23</sup>. The core of two TDs relaxes on slanted planes to form a coherency disclination, which bonds  $\{\bar{1}011\}$  pyramidal plane in twin and  $\{0002\}$  basal plane in matrix (referred to as  $\text{Py}_1/\text{B}$ ) for ( $\mathbf{b}_T, h_0$ ), or vice versa in matrix (referred to as  $\text{B}/\text{Py}_1$ ) for ( $-\mathbf{b}_T, -h_0$ ). Due to the lattice mismatch between pyramidal and basal planes, coherency stress develops in the core, tension in basal plane and compression in pyramidal plane for Mg<sup>3,26</sup>. Thus, the local stress field (details in Supplementary Note 1 and Supplementary Fig. 1) destroys the two-fold symmetry of the dislocation about the rotation axis  $\mathbf{K}_1$ . In comparison, Fig. 2c shows atomic structure of a TD dipole in DS view where TDs are screw type. Two TDs have planar-extended core structures. The two planes in twin and matrix have the same crystallographic index, thus zero coherency stress is developed.

We further calculated the energy change (Fig. 2d) and the Peach-Koehler (P-K) resistance force<sup>7</sup> (Fig. 2e) associated with the motion of ( $\mathbf{b}_T, h_0$ ) (right TDs in Fig. 2b, c). In the figure,  $\mathbf{x}$  is the position of TD with respect to its initial position (Fig. 2b, c). The value  $l$  is the periodic distance along  $-\eta_1$  or  $\lambda$  directions. Therefore,  $\mathbf{x}/l$  is the relative position of ( $\mathbf{b}_T, h_0$ ). An increase in relative position  $\mathbf{x}/l$  indicates the motion of TD along  $-\eta_1$  or  $\lambda$  direction (causes twinning), and vice versa. The energy change profile (black curve in Fig. 2d) does not retain symmetry along  $\eta_1$  and  $-\eta_1$  directions. The P-K force (black curve in Fig. 2e) in  $-\eta_1$  direction is  $0.44 \text{ N m}^{-1}$ , lower than that in  $\eta_1$  direction ( $0.53 \text{ N m}^{-1}$ ). Thus, the difference in resistance force ( $0.09 \text{ N m}^{-1}$ ) corresponds to the difference of  $0.79 \text{ GPa}$  in required resolved shear stress (RSS). In comparison, the energy change profile (red curve in Fig. 2d) is symmetric and the corresponding resistance force (red curve in Fig. 2e) is the same for TD motion in the  $\lambda$  and  $-\lambda$  directions. Atomistic simulation shows that single edge TD is easier to propagate along the  $-\eta_1$  direction than  $\eta_1$  direction while single screw TD along  $\lambda$  and  $-\lambda$  direction is subject to the same resistance force.

Multiple TDs ( $\mathbf{b}_T, h_0$ ) piling up on specific crystal plane<sup>3</sup> can be treated as a super-disconnection ( $n\mathbf{b}_T, nh_0$ ) which often relaxes into a low energy facet, described by "A/B" facet ("A" and "B" represents the crystal plane in twin and matrix) and recently named as coherency disclination<sup>17</sup>. For example, as demonstrated by experimental observation<sup>19,27,28</sup> and MD simulations<sup>25,29</sup>, P/B and B/P facets of  $\{10\bar{1}2\}$  twin bonds the prismatic and basal interfaces and  $\text{Py}_1/\text{B}$  and  $\text{B}/\text{Py}_1$  of  $\{10\bar{1}1\}$  twin bonds pyramidal and basal planes. These A/B facets have disclination character and can glide as entities<sup>30</sup>. A disclination can be decomposed into three components (wedge, twist, and misfit components in Supplementary Note 1 and Supplementary Fig. 1a). Types of disclinations with different components and their corresponding stress fields have implication on the symmetric/asymmetric kinetics of disclinations (details in Supplementary Note 1 and Supplementary Fig. 1b–g).

We further investigated the mobility of facets along twinning and detwinning directions which depends on facet index. Prediction of the facets starts with the coherent dichromatic complex (CDC). In BS view (Fig. 3a), there are three possible

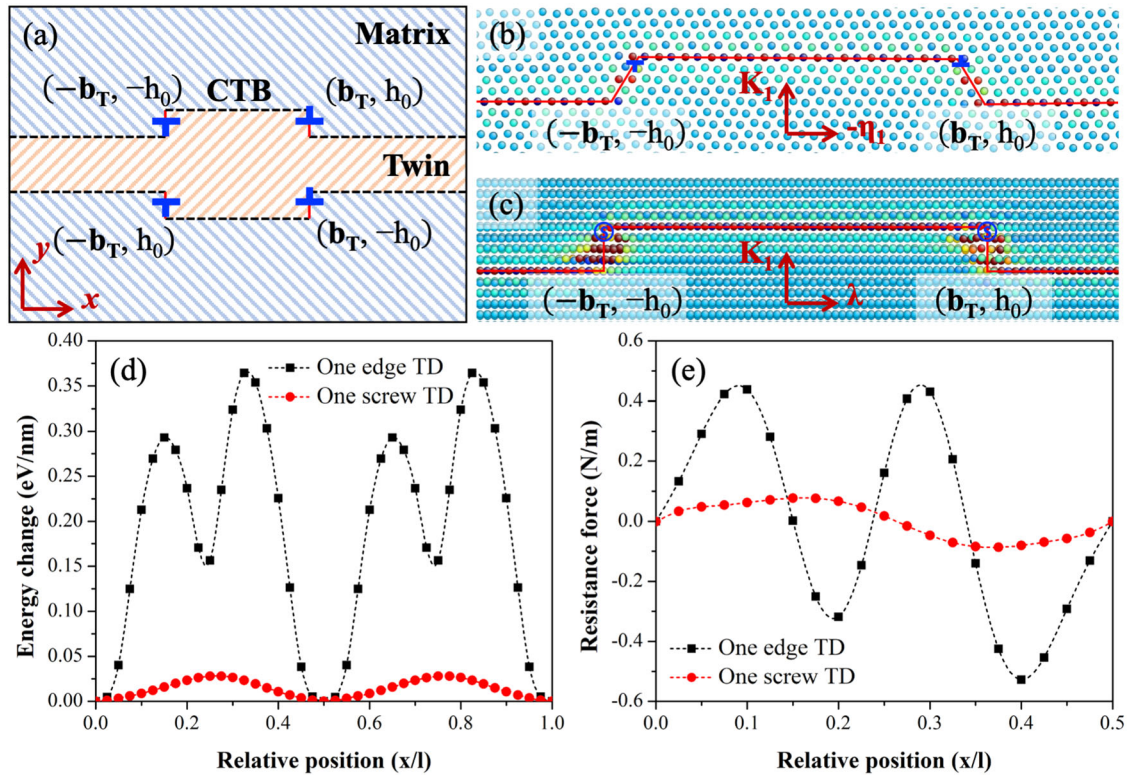


**Fig. 2 Structures and kinetics of single TD.** **a** Schematics showing TDs along CTBs. **b** Atomic structure of a pure edge TD dipole in BS view. **c** Atomic structure of a pure screw TD dipole in DS view. **d** The change of potential energy associated with the migration of an edge TD and a screw TD. **e** The resistance force associated with the migration of an edge TD and a screw TD.

interfaces, which are  $\{0002\}_{M/T}||\{\bar{1}011\}_{T/M}$  (B/Py<sub>1</sub>) interface,  $\{10\bar{1}0\}_{M/T}||\{10\bar{1}3\}_{T/M}$  (Pr<sub>1</sub>/Py<sub>2</sub>) interface, and conjugate TB  $\{\bar{1}013\}_{M/T}||\{10\bar{1}3\}_{T/M}$  (K<sub>2</sub>/K<sub>2</sub>). In DS view (Fig. 3b),  $\{\bar{1}2\bar{1}0\}_{M/T}||\{\bar{1}2\bar{1}0\}_{T/M}$  (Pr<sub>2</sub>/Pr<sub>2</sub>) interface,  $\{02\bar{2}1\}_{M/T}||\{02\bar{2}1\}_{T/M}$  (Py<sub>3</sub>/Py<sub>3</sub>) interface, and  $\{4223\}_{M/T}||\{4223\}_{T/M}$  (Py<sub>4</sub>/Py<sub>4</sub>) interface are possible. Using atomistic simulations, we calculated formation energies, and analyzed kinetics of these possible facets. In BS view, facets in Fig. 3c–e are stable. The line energy associated with B/Py<sub>1</sub> or Py<sub>1</sub>/B and K<sub>2</sub>/K<sub>2</sub> facets are almost the same and lower than that associated with Pr<sub>1</sub>/Py<sub>2</sub> or Py<sub>2</sub>/Pr<sub>1</sub> facet (Supplementary Note 2 and Supplementary Fig. 2a). K<sub>2</sub>/K<sub>2</sub> facet first transforms to discrete TDs and then migrates. Therefore, B/Py<sub>1</sub> or Py<sub>1</sub>/B facet is favored based on both energetic and kinetic consideration in BS view. In contrast, the facets in DS view in Fig. 3f–h, manifest only Pr<sub>2</sub>/Pr<sub>2</sub> facet is stable (Supplementary Note 1 and Supplementary Fig. 2b), and other facets degenerate into discrete TDs.

The energy change and the resistance force associated with the motion of the 8-layer thick Py<sub>1</sub>/B and Pr<sub>2</sub>/Pr<sub>2</sub> facets with two TDs (Supplementary Note 2 and Supplementary Fig. 2c, d) share similar features to those shown in Fig. 2d, e with single TD, indicating asymmetric kinetics of Py<sub>1</sub>/B facets and symmetric kinetics of Pr<sub>2</sub>/Pr<sub>2</sub> facets. As shown in Fig. 3i, when more TDs are involved, the kinetic barrier associated with migration of the Py<sub>1</sub>/B facet with edge TDs greatly increases while the kinetic barrier associated with migration of the Pr<sub>2</sub>/Pr<sub>2</sub> facet with screw TDs slightly increases. Figure 3j exhibits the difference in resistance force with respect to the number of TDs on a facet. For motion of screw TDs, the difference in force is nearly zero. For motion of edge TDs along, the difference in force associated with motion of an 8-layer thick Py<sub>1</sub>/B facet (with two TDs) increases to  $0.20 \text{ N m}^{-1}$  from  $0.09 \text{ N m}^{-1}$  of a 4-layer step (with single TD). Correspondingly, the difference in required RSS is 0.88 GPa for an 8-layer thick Py<sub>1</sub>/B facet and 0.79 GPa for a 4-layer Py<sub>1</sub>/B step. Thus, the asymmetric

kinetics of edge TDs becomes more obvious when more TDs pile up to form longer facet.

The symmetric/asymmetric kinetics of facets eventually affects the shape of twins. Figure 3k, l schematically shows a twin embedded in the matrix in the coordinate that y-axis is along  $\mathbf{K}_1$  direction and x-axis is the migration direction of steps/facets. On  $\pm\mathbf{K}_1$  planes, terraces that consist of CTBs and facets may form. Based on crystallography associated with compound twins, a twin orientation is obtained by a 180° rotation about either  $\mathbf{K}_1$  or  $\eta_1$  direction. If x-axis is along  $-\eta_1$  direction (Fig. 3k), atomistic simulations suggest that long Py<sub>1</sub>/B facets have higher mobility during twinning than that during detwinning. Consequently, during twinning, A/B facets migrate faster than B/A facets, causing lath-shaped twins with asymmetric twin tips. In comparison, if x-axis is along  $\lambda$  direction (Fig. 3l), planes in matrix and twin have the same index (A/A type facet), atom displacements during motion of such facet along  $\lambda$  and  $-\lambda$  directions are equivalent. Moreover, we may speculate that A/A type facets that contain wedge and/or twist disclination components also have the same mobility when migrating in the opposite directions because the core structures retain the two-fold symmetry about the rotation axis  $\mathbf{K}_1$  (i.e., Supplementary Fig. 1c, f). In this scenario, twins may exhibit lenticular shape with symmetric twin tips in lateral DS view while exhibit lath-shape with asymmetric twin tips in forward BS view. These speculations can be validated by TEM characterization of twin facets and twin shape in different directions.

### Microscopy evidence of symmetric/asymmetric twinning

Microscopy characterization shows a lath-shaped  $(10\bar{1}1)$  twin domain in BS view (Fig. 4). For simplicity, the boundaries toward  $\pm\mathbf{K}_1$  and  $\pm\eta_1$  directions are denoted. Two purple points, as marked the apexes along  $\mathbf{K}_1$  in Fig. 4a, do not lie on the same axis. Furthermore, the twin tips as shown in Fig. 4b, c exhibit

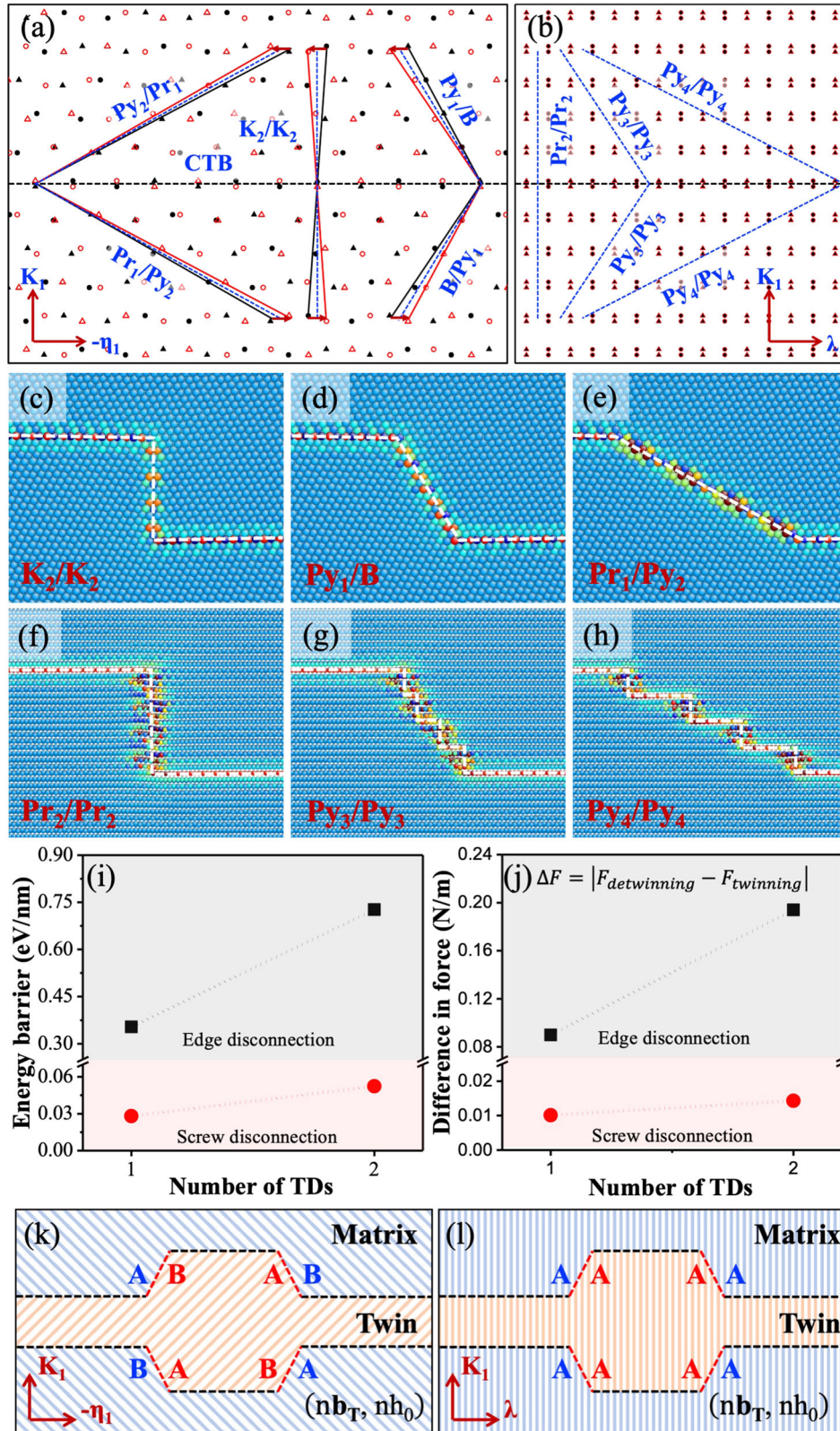


**Fig. 3 Structures and kinetics of twin facets.** CDC associated with  $\{10\bar{1}1\}$  twinning **a** viewed along  $\lambda$  direction predicts the B/Py<sub>1</sub> or Py<sub>1</sub>/B, Pr<sub>1</sub>/Py<sub>2</sub> or Py<sub>2</sub>/Pr<sub>1</sub> and K<sub>2</sub>/K<sub>2</sub> interfaces, and **b** viewed along  $-\eta_1$  direction predicts the Pr<sub>2</sub>/Pr<sub>2</sub>, Py<sub>3</sub>/Py<sub>3</sub> and Py<sub>4</sub>/Py<sub>4</sub> interfaces. Relaxed structures containing **c** K<sub>2</sub>/K<sub>2</sub> facet, **d** Py<sub>1</sub>/B facet, and **e** Pr<sub>1</sub>/Py<sub>2</sub> facet in BS view. Relaxed structures containing **f** Pr<sub>2</sub>/Pr<sub>2</sub> facet, **g** Py<sub>3</sub>/Py<sub>3</sub> facet, and **h** Py<sub>4</sub>/Py<sub>4</sub> facet in DS view. **i** The change of potential energy associated with the migration of a Py<sub>1</sub>/B or a Pr<sub>2</sub>/Pr<sub>2</sub> facet with respect to the number of edge or screw TDs on the facet. **j** Difference in resistance force associated with the migration of a Py<sub>1</sub>/B or Pr<sub>2</sub>/Pr<sub>2</sub> facet along twinning and detwinning directions with respect to number of edge or screw TDs on the facet. Schematics showing terraces on CTBs consisting of **k** CTBs, A/B and B/A facets in BS view and **l** CTBs and A/A facets in DS view.

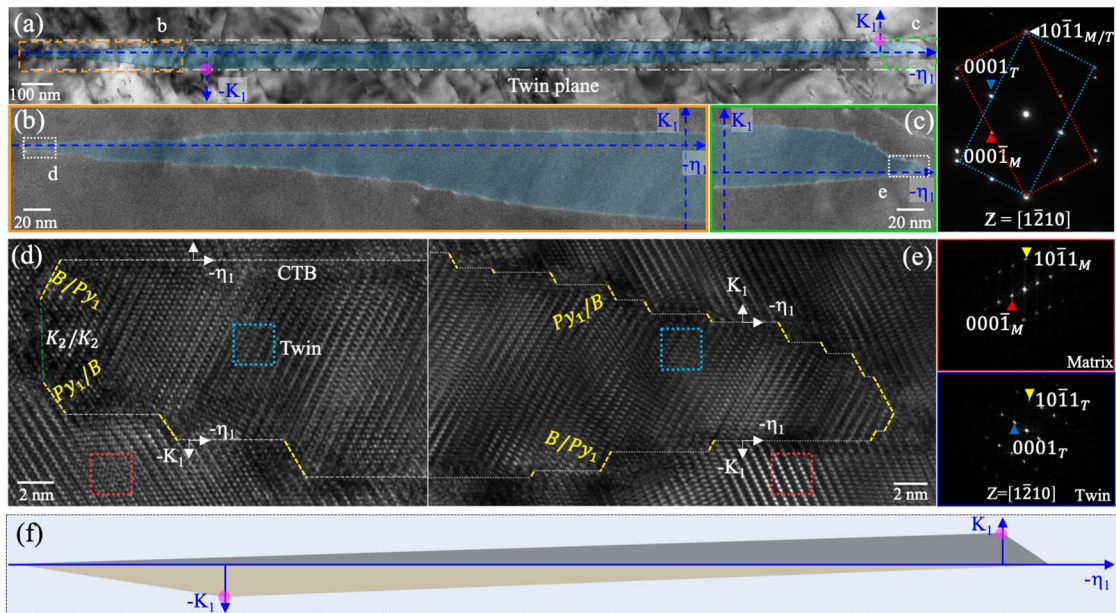


**Fig. 4** TEM micrographs of a  $(10\bar{1}1)$  twin in  $[1\bar{2}10]$  (BS) view. **a** A lath-shaped twin domain in low magnification image. The inset is the SADP confirming the  $[1\bar{2}10]$  observation direction and  $(10\bar{1}1)$  twin orientation. The HAADF image showing the **b**  $\eta_1$  ( $[10\bar{1}2]$  direction) twin tip and **c**  $-\eta_1$  ( $[\bar{1}012]$  direction) twin tips enclosed by the green rectangles in **a** respectively. **d**, **e** High magnification images of the regions enclosed by the orange rectangles in **b** and **c** showing asymmetric twin tips comprising CTBs,  $K_2/K_2$ , B/Py<sub>1</sub> and Py<sub>1</sub>/B facets. The insets are the FFT of the regions enclosed by the red and blue squares, confirming the matrix and twin orientation. **f** Schematic showing the geometric shape of  $(10\bar{1}1)$  twins in BS view.

asymmetry shape about  $\pm\eta_1$  direction. Figure 4d, magnified high-resolution TEM image from Fig. 4b, manifesting CTBs (white line),  $K_2/K_2$  (green line), Py<sub>1</sub>/B and B/Py<sub>1</sub> (yellow line) facets. More Py<sub>1</sub>/B facets on  $-K_1$  (bottom) than B/Py<sub>1</sub> facets on  $K_1$  (top), explaining the greater deviation of the  $-K_1$  boundary from twin plane. In contrast, more Py<sub>1</sub>/B facets on  $K_1$  than B/Py<sub>1</sub> facets on  $-K_1$ , resulting a greater deviation of the  $K_1$  boundary from on the other side of the same twin domain (Fig. 4c, e). Both asymmetry along  $K_1$  axis and twin tip along  $\eta_1$  axis are highlighted in Fig. 4f. The experimental evidence suggests that Py<sub>1</sub>/B facets have higher mobility than B/Py<sub>1</sub> facets during twinning.

In DS view, twin and matrix are identical, where TDs is hard to distinguish at atomic level. However, twin boundaries can be roughly identified at low magnification with aid of local contrast differences, and an overall symmetric twin tip is observed (Supplementary Note 3 and Supplementary Fig. 3). Since characterization of twin facets at atomic resolution remains challenging, alternatively, we characterized A/A type  $(1\bar{1}01)_{T/M} \parallel (1\bar{1}01)_{M/T}$  (Py<sub>1</sub>/Py<sub>1</sub>) facets which can be found in  $[0\bar{1}11]$  view (Supplementary Note 3 and Fig. 4). The twin as shown in Fig. 5a exhibits a lenticular-shaped domain. Two purple points mark the  $\pm K_1$  apexes lie on the same axis. This indicates  $(10\bar{1}1)$  twin can symmetrically propagate along non  $\pm\eta_1$  direction (here:  $\pm[5\bar{6}14]$ ). The twin tip in Fig. 5b is symmetric about  $[5\bar{6}14]$  direction. HRTEM in Fig. 5c, d displays two regions magnified from Fig. 5b with similar numbers and heights of Py<sub>1</sub>/Py<sub>1</sub> facets on  $\pm K_1$  boundaries, indicating a symmetric kinetics of the A/A type Py<sub>1</sub>/Py<sub>1</sub> facets along  $\pm[5\bar{6}14]$  directions.

Experimental characterizations well demonstrate asymmetric propagation of TDs. During twinning, mobility of Py<sub>1</sub>/B facets (A/B type) is higher than that of B/Py<sub>1</sub> facets. As a result, more Py<sub>1</sub>/B facets are observed near both twin tips. The outcome is a lath-shaped twin which is not symmetric about neither  $K_1$  nor  $\eta_1$  direction. Meanwhile, the distribution of Py<sub>1</sub>/Py<sub>1</sub> facets (A/A type) on  $\pm K_1$  boundaries should be nearly symmetric about both  $K_1$  and  $\eta_1$  direction, thus, a lenticular-shaped twin can be observed.

Moreover, microscopy characterization of  $\{10\bar{1}2\}$  twin shows lenticular-shaped domain in both BS and DS views (Supplementary Note 4 and Fig. S5), with B/P (A/B type) facets<sup>22</sup>. This discrepancy is attributed to the small difference in Peierls barriers for the elementary TD in  $\{10\bar{1}2\}$  twins. Resistance forces for the glide of elementary TD in the  $\eta_1$  and  $-\eta_1$  direction on  $K_1$  plane are  $0.876 \times 10^{-2} \text{ N m}^{-1}$  and  $1.280 \times 10^{-2} \text{ N m}^{-1}$  for  $\{10\bar{1}2\}$  twinning. Correspondingly, for edge  $\{10\bar{1}2\}$  and  $\{10\bar{1}1\}$  TDs, the difference in required RSS is 0.082 GPa for edge  $\{10\bar{1}2\}$  TD, which is far smaller than 0.79 GPa for edge  $\{10\bar{1}1\}$  TD.

## DISCUSSION

The glide resistance to TDs with both dislocation and step character is mainly accounted for based on the dislocation character, and widely recognized to be symmetric, i.e., the same for the forward and backward motion. Here, we for the first time reveal the influence of step character on the core structure of TDs. Correspondingly, a TD can be described with A/A type or A/B type coherency disclination. We further demonstrate the A/B type TD glides with asymmetric resistance in the forward and backward motion, while the A/A type TD glides with same resistance. With this knowledge, we successfully account for the formation of asymmetric and symmetric twin tips of  $\{10\bar{1}1\}$  and  $\{10\bar{1}2\}$  twins in Mg alloys.

Our work enriches the fundamental understanding of twinning mechanisms, may help develop the strategy of controlling twinning in hexagonal metals via tailoring core structure of TDs via solutes<sup>31–33</sup>. More importantly, the findings of symmetric and asymmetric glide resistance to A/A type and A/B type TDs can be directly incorporated into multiscale materials modeling tools. For example, phase field model can predict 3D twin growth by integrating mobilities of twin facets calculated by atomistic simulations<sup>34</sup>. The mobilities of A/B and B/A twin facets, i.e., B/P and P/B facets of  $\{10\bar{1}2\}$  twinning, are treated the same. Our findings suggest that mobilities of A/B and B/A twin facets should

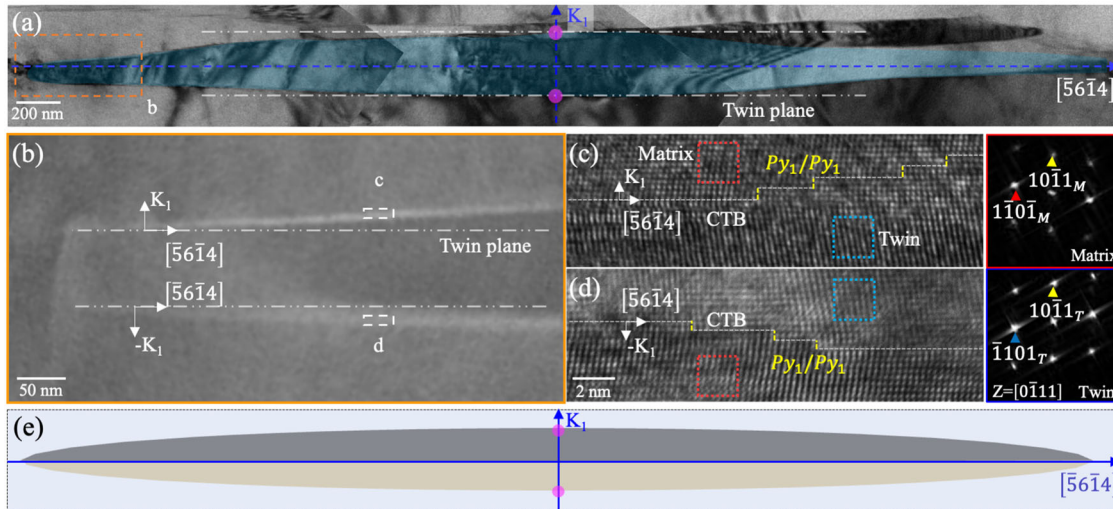


**Fig. 5** TEM micrographs of a  $(10\bar{1}1)$  twin in  $[0\bar{1}11]$  view. **a** A lenticular-shaped twin domain in low magnification image. **b** The HAADF image showing the twin tip enclosed by the orange rectangle in **a**. **c, d** High magnification images of the regions enclosed by the white rectangles in **b** showing  $Py_1/Py_2$  facets on  $\pm K_1$  boundaries. The insets are the FFT of the regions enclosed by the red and blue squares, confirming the matrix and twin orientation. **e** Schematic showing the geometric shape of  $(10\bar{1}1)$  twin in  $[0\bar{1}11]$  view.

be evaluated separately for twinning other than  $\{10\bar{1}2\}$  twinning. In addition, grain boundary dynamics are largely controlled by the formation and motion of disconnections along with the GB<sup>35</sup>. The symmetric/asymmetric mobilities can be directly incorporated into the available continuum models for grain boundary migration based on disconnections<sup>36,37</sup>.

## METHODS

### Atomistic simulations

Molecular static/dynamics (MS/MD) simulations were conducted for Mg with the empirical interatomic potential developed by Liu et al.<sup>30</sup>. The construction of models containing steps/facets in BS view starts with an  $80 \times 80 \times 1.60$  nm bicrystal with  $(\bar{1}011)$  twin orientation in the coordinate that x-axis is along  $-\eta_1$  (in  $[10\bar{1}2]$  direction), y-axis is along  $K_1$  (normal to  $(\bar{1}011)$  plane), and z-axis is along  $-\lambda$  (in  $[1\bar{2}10]$  direction). To create a  $4n$ -layer step/facet,  $n$  pure edge TDs with Burgers vector  $(-0.133, 0, 0)$  nm are introduced on every four  $(\bar{1}011)$  layers by applying anisotropic Barnett-Lothe solutions<sup>38</sup> followed by atoms shuffles. Similarly, an  $80 \times 80 \times 2.352$  nm bicrystal with  $(\bar{1}011)$  twinning orientation in the coordinate that x-axis is along  $\lambda$  (in  $[\bar{1}2\bar{1}0]$  direction), y-axis is along  $K_1$  (normal to  $(\bar{1}011)$  plane), and z-axis is along  $-\eta_1$  (in  $[10\bar{1}2]$  direction) is adopted to construct models containing steps/facets in DS view. After introducing  $n$  pure screw TDs with Burgers vector  $(0, 0, -0.133)$  nm and corresponding shuffling, a  $4n$ -layer step/facet is constructed. To relax steps/facets in both BS and DS views, dynamic quenching is performed until the maximum force is  $<5$  pN with fixed boundaries in x- and y-direction and periodic boundary condition in z-direction.

The energy barrier associated with the motion of TDs is calculated by Nudge Elastic Band (NEB) method<sup>39</sup> with 39 intermediate states. The displacement between the steps/facets in the initial and final configurations is defined as  $l$ , which is along  $-\eta_1$  direction with magnitude 1.18 nm for edge TDs and along  $\lambda$  direction with magnitude 0.32 nm for screw TDs. The NEB calculations are converged until the difference in the total energy within 10 iterative steps is  $<10^{-3}$  eV. Peach-Koehler force<sup>7</sup> is derived by differentiating the energy curve with respect the moving distance within the range from 0 to  $l/2$ . The RSS required to overcome the barrier is estimated through dividing the resistance force by the magnitude of Burgers vector of TDs.

### Materials preparation and characterization

The Mg-0.2 at. % Gd ingot specimens were used for the present investigation. The specimens were firstly extruded at 300 °C. The as-extruded specimens were compressed by 8% at room temperature along the extrusion direction. For high-annular dark-field scanning transmission

electron microscope (HAADF-STEM) characterization, sequential aging (275 °C for 1 h) was carried out for twin boundary Gd atom segregation. Details of HAADF characterization method is described in ref. 19. For  $\bar{1}210$  and  $0\bar{1}11$  direction observation, perforation of 3 mm disk specimen (former polished to a thickness of  $\sim 40$   $\mu\text{m}$ ) by ion milling was carried out with low-angle ( $3^\circ$ ) and low energy (3 keV) ion-beam. High-resolution transmission electron microscope (HRTEM) and HAADF-STEM were carried out on a JEOL-2100F electron microscope with a voltage of 200 kV. The lattice constant ( $a = b = 3.21$  Å,  $c = 5.21$  Å,  $\alpha = \beta = 90^\circ$ ,  $\gamma = 120^\circ$ ) is selected for pole figure and diffraction pattern analysis of  $\{10\bar{1}1\}$  twin in Mg.

## DATA AVAILABILITY

The data sets generated during and/or analyzed during the current study are available from the corresponding author on reasonable request.

Received: 24 April 2022; Accepted: 26 July 2022;  
Published online: 16 August 2022

## REFERENCES

- Howe, J. M., Pond, R. C. & Hirth, J. P. The role of disconnections in phase transformations. *Prog. Mater. Sci.* **54**, 792–838 (2009).
- Hirth, J. P. & Pond, R. C. Steps, dislocations and disconnections as interface defects relating to structure and phase transformations. *Acta Mater.* **44**, 4749–4763 (1996).
- Hirth, J. P., Wang, J. & Tomé, C. N. Disconnections and other defects associated with twin interfaces. *Prog. Mater. Sci.* **83**, 417–471 (2016).
- Furuhara, T., Chiba, T., Kaneshita, T., Wu, H. & Miyamoto, G. Crystallography and interphase boundary of martensite and bainite in steels. *Metall. Mater. Trans. A* **48**, 2739–2752 (2017).
- Aaronson, H. I. et al. On the mechanism of formation of diffusional plate-shaped transformation products. *Acta Mater.* **54**, 1227–1232 (2006).
- Khater, H. A., Serra, A. & Pond, R. C. Atomic shearing and shuffling accompanying the motion of twinning disconnections in Zirconium. *Philos. Mag.* **93**, 1279–1298 (2013).
- Hirth, J. P. & Lothe, J. *Theory of Dislocations*, 2nd edn. (Hohn Wiley and Son, New York, 1982).
- Mitchell, T. E. & Hirth, J. P. The shape, configuration and stress field of twins and martensite plates. *Acta Metall. Mater.* **39**, 1711–1717 (1991).
- Pond, R. C. & Hirth, J. P. 3D defect structure of products in displacive phase transformations. *J. Alloy Compd.* **577**, S710–S712 (2013).
- Aaronson, H. I., Howe, J. M., Hall, M. G., Furuhrara, T. & Hirth, J. P. Mobility of structural ledges. *Scr. Mater.* **37**, 1301–1307 (1997).



11. Hirth, J. P. & Pond, R. C. Compatibility and accommodation in displacive phase transformations. *Prog. Mater. Sci.* **56**, 586–636 (2011).
12. Wang, J., Hirth, J. P. & Tomé, C. N.  $\{10\bar{1}2\}$  Twinning nucleation mechanisms in hexagonal-close-packed crystals. *Acta Mater.* **57**, 5521–5530 (2009).
13. Wang, J., Liu, L., Tomé, C. N., Mao, S. X. & Gong, S. K. Twinning and de-twinning via glide and climb of twinning dislocations along serrated coherent twin boundaries in hexagonal-close-packed metals. *Mater. Res. Lett.* **1**, 81–88 (2013).
14. Wang, J., Beyerlein, I. J., Hirth, J. P. & Tomé, C. N. Twinning dislocations on  $\{1\bar{1}011\}$  and  $\{1\bar{1}013\}$  planes in hexagonal close-packed crystals. *Acta Mater.* **59**, 3990–4001 (2011).
15. Christian, J. W. & Mahajan, S. Deformation twinning. *Prog. Mater. Sci.* **39**, 1–157 (1995).
16. Serra, A., Bacon, D. J. & Pond, R. C. The crystallography and core structure of twinning dislocations in H.C.P. metals. *Acta Metall.* **36**, 3183–3203 (1988).
17. Hirth, J. P., Hirth, G. & Wang, J. Disclinations and disconnections in minerals and metals. *Proc. Natl Acad. Sci. USA* **117**, 196 (2020).
18. Wang, J., Beyerlein, I. J. & Hirth, J. P. Nucleation of elementary  $\{1\bar{1}011\}$  and  $\{1\bar{1}013\}$  twinning dislocations at a twin boundary in hexagonal close-packed crystals. *Model. Simul. Mater. Sci. Eng.* **20**, 024001 (2012).
19. Zhu, Y. M., Xu, S. W. & Nie, J. F.  $\{10\bar{1}1\}$  Twin boundary structures in a Mg–Gd alloy. *Acta Mater.* **143**, 1–12 (2018).
20. Pond, R. C., Hirth, J. P., Serra, A. & Bacon, D. J. Atomic displacements accompanying deformation twinning: shears and shuffles. *Mater. Res. Lett.* **4**, 185–190 (2016).
21. Liu, Y. et al. Characterizing the boundary lateral to the shear direction of deformation twins in magnesium. *Nat. Commun.* **7**, 11577 (2016).
22. Liu, Y. et al. Three-dimensional character of the deformation twin in magnesium. *Nat. Commun.* **10**, 3308 (2019).
23. Serra, A., Pond, R. C. & Bacon, D. J. Computer simulation of the structure and mobility of twinning dislocations in H.C.P. metals. *Acta Metall. Mater.* **39**, 1469–1480 (1991).
24. Gong, M. et al. Steps and  $\{11\bar{2}1\}$  secondary twinning associated with  $\{11\bar{2}2\}$  twin in titanium. *Acta Mater.* **164**, 776–787 (2019).
25. Xu, B., Capolungo, L. & Rodney, D. On the importance of prismatic/basal interfaces in the growth of  $\{10\bar{1}2\}$  twins in hexagonal close packed crystals. *Scr. Mater.* **68**, 901–904 (2013).
26. Wang, J., Yadav, S. K., Hirth, J. P., Tomé, C. N. & Beyerlein, I. J. Pure-Shuffle nucleation of deformation twins in hexagonal-close-packed metals. *Mater. Res. Lett.* **1**, 126–132 (2013).
27. Liu, B. Y. et al. Twinning-like lattice reorientation without a crystallographic twinning plane. *Nat. Commun.* **5**, 3297 (2014).
28. Sun, Q., Zhang, X., Ren, Y., Tu, J. & Liu, Q. Interfacial structure of  $\{10\bar{1}2\}$  twin tip in deformed magnesium alloy. *Scr. Mater.* **90**, 41–44 (2014).
29. Barrett, C. D. & El Kadiri, H. Impact of deformation faceting on  $\{10\bar{1}2\}$ ,  $\{10\bar{1}1\}$  and  $\{10\bar{1}3\}$  embryonic twin nucleation in hexagonal close-packed metals. *Acta Mater.* **70**, 137–161 (2014).
30. Gong, M., Hirth, J. P., Liu, Y., Shen, Y. & Wang, J. Interface structures and twinning mechanisms of twins in hexagonal metals. *Mater. Res. Lett.* **5**, 449–464 (2017).
31. Nie, J. F., Zhu, Y. M., Liu, J. Z. & Fang, X. Y. Periodic segregation of solute atoms in fully coherent twin boundaries. *Science* **340**, 957–960 (2013).
32. Zhu, Y. M., Bian, M. Z. & Nie, J. F. Tilt boundaries and associated solute segregation in a Mg–Gd alloy. *Acta Mater.* **127**, 505–518 (2017).
33. Kumar, A., Wang, J. & Tomé, C. N. First-principles study of energy and atomic solubility of twinning-associated boundaries in hexagonal metals. *Acta Mater.* **85**, 144–154 (2015).
34. Gong, M., Graham, J., Taupin, V. & Capolungo, L. The effects of stress, temperature and facet structure on growth of  $\{10\bar{1}2\}$  twins in Mg: a molecular dynamics and phase field study. *Acta Mater.* **208**, 116603 (2021).
35. Han, J., Thomas, S. L. & Srolovitz, D. J. Grain-boundary kinetics: a unified approach. *Prog. Mater. Sci.* **98**, 386–476 (2018).
36. Zhang, L., Han, J., Xiang, Y. & Srolovitz, D. J. Equation of motion for a grain boundary. *Phys. Rev. Lett.* **119**, 246101 (2017).
37. Zhang, L., Han, J., Srolovitz, D. J. & Xiang, Y. Equation of motion for grain boundaries in polycrystals. *npj Comput. Mater.* **7**, 1–8 (2021).
38. Barnett, D. M. & Lothe, J. An image force theorem for dislocations in anisotropic bicrystals. *J. Phys. F.* **4**, 1618 (1974).
39. Henkelman, G. & Jónsson, H. Improved tangent estimate in the nudged elastic band method for finding minimum energy paths and saddle points. *J. Chem. Phys.* **113**, 9978–9985 (2000).

## ACKNOWLEDGEMENTS

Access to the microscopes at the state key labs of Metal Matrix Composites at Shanghai Jiao Tong University is acknowledged. Discussion with Prof. John P. Hirth is greatly appreciated.

## AUTHOR CONTRIBUTIONS

Y.L. and J.W. conceived the project. M.G. performed the atomistic simulations. J.-F.N. prepared the materials. H.M. and K.Y. obtained TEM data. Y.L., J.W., M.G., and H.M. prepared the first draft of this manuscript, and all authors participated the discussion and writing of this manuscript.

## COMPETING INTERESTS

The authors declare no competing interests.

## ADDITIONAL INFORMATION

**Supplementary information** The online version contains supplementary material available at <https://doi.org/10.1038/s41524-022-00855-y>.

**Correspondence** and requests for materials should be addressed to Yue Liu or Jian Wang.

**Reprints and permission information** is available at <http://www.nature.com/reprints>

**Publisher's note** Springer Nature remains neutral with regard to jurisdictional claims in published maps and institutional affiliations.



**Open Access** This article is licensed under a Creative Commons Attribution 4.0 International License, which permits use, sharing, adaptation, distribution and reproduction in any medium or format, as long as you give appropriate credit to the original author(s) and the source, provide a link to the Creative Commons license, and indicate if changes were made. The images or other third party material in this article are included in the article's Creative Commons license, unless indicated otherwise in a credit line to the material. If material is not included in the article's Creative Commons license and your intended use is not permitted by statutory regulation or exceeds the permitted use, you will need to obtain permission directly from the copyright holder. To view a copy of this license, visit <http://creativecommons.org/licenses/by/4.0/>.

© The Author(s) 2022